This is a preprint, the final version is subject to change, of the American Mineralogist (MSA)
Cite as Authors (Year) Title. American Mineralogist, in press.
(DOI will not work until issue is live.) DOI: http://dx.doi.org/10.2138/am-2017-5853

1

2 **Revision 2**

3 # A new high pressure phase transition in clinoferrosilite: in situ single crystal
4 # X-ray diffraction study.

5 Anna Pakhomova*, Leyla Ismailova, Elena Bykova, Mazim Bykov, Tiziana Boffa Ballaran,

6 Leonid Dubrovinsky

7 * a.s.pakhomova@mail.ru, Bayerisches Geoinstitute, University of Bayreuth, Universitätsstraße
8 30, D-95447 Bayreuth, Germany

9 **Abstract**

10 Synchrotron-based high-pressure single-crystal X-ray diffraction experiments were conducted on
11 synthetic pure clinoferrosilite, $Fe_2Si_2O_6$, at room temperature to a maximum pressure of 45 GPa.
12 In addition to the previously described $P2_1/c \rightarrow C2/c$ phase transition between 1.48 and 1.75 GPa
13 (Hugh-Jones et al., 1994), we observe further transition between 30 and 36 GPa into the high-
14 pressure $P2_1/c$ phase (HP-$P2_1/c$). The $C2/c \rightarrow$HP-$P2_1/c$ transition is induced by rearrangement of
15 half of the layers of corner-sharing SiO_4 tetrahedra into layers of edge-sharing SiO_6 octahedra.
16 The new configuration of ^{VI}Si layers suggests a possibility of a progressive transformation of the
17 pyroxene into an ilmenite-type structure. The persistence of metastable pyroxene up to pressures
18 higher than expected and its feasible direct transformation to ilmenite are of special interest for
19 understanding the dynamics of cold subducting slabs. We report on structural and
20 compressibility features of both high-pressure phases as well as address thermal stability of HP-
21 $P2_1/c$.

22

23 **Keywords:** pyroxene, single-crystal X-ray diffraction, high-pressure, high-temperature, phase
24 transitions

This is a preprint, the final version is subject to change, of the American Mineralogist (MSA)
Cite as Authors (Year) Title. American Mineralogist, in press.
(DOI will not work until issue is live.) DOI: http://dx.doi.org/10.2138/am-2017-5853

Introduction

Pyroxenes belonging to the $CaFeSi_2O_6$ (hedenbergite, Hd) – $MgCaSi_2O_6$ (diopside, Di) - $Fe_2Si_2O_6$ (ferrosilite, Fs) – $Mg_2Si_2O_6$ (enstatite, En) quadrilateral system (Morimoto *et al*., 1989) are one of the major constituent minerals in the Earth's upper mantle. Depending on the assumed petrological model, orthopyroxenes compose from 17 to 27 % of the upper mantle whereas the content of clinopyroxenes varies in the range 16-20% (Frost, 2008). The significant proportion of pyroxenes results in their inevitable influence on mineralogy, thermodynamics and geological structure of the upper mantle. Phase transitions in pyroxenes have been repetitively considered as a possible cause or contribution to seismic discontinuities in the mantle such as the Lehmann and the X shallow discontinuities (Woodland, 1998; Deuss and Woodhouse, 2002; Stixrude and Lithgow-Bertelloni, 2005; Akashi et al., 2009; Jacobsen et al., 2010; Ferot and Bolfan-Casanova, 2012). Pyroxenes are also a major constituent of the harzburgites that make up a large portion of subducting lithosphere (Ringwood, 1982). Under relatively cold temperatures (in comparison with the mantle geotherm away from tectonic plate boundary) of subducting slabs, pyroxenes may be retained down to transition zone depths through slower subduction and/or transient stagnation (Mierlo et al., 2013; Agrusta et al., 2014) as metastable phases add buoyancy to the slabs. Under such conditions, the direct transformation of pyroxene to a dense ilmenite-type phase may occur, possibly promoting penetration of stagnant slab into the lower mantle (Hogrefe et al., 1994).

The occurrence of pyroxenes in different geological locations as well as their rich high-temperature - high-pressure phase diagram may be explained by the flexibility of their crystal structures, which are composed of cubic close-packed layers of O atoms with alternating tetrahedral and octahedral layers (Fig. 1). The octahedral M1 and M2 sites can accommodate a variety of different cations (*e.g.* Mg^{2+}, Fe^{2+}, Ca^{2+}, Mn^{2+}, Na^{+}, Al^{3+}, Fe^{3+}, Cr^{3+}) as well as vacancies (McCormick, 1986; Ma et al., 2015) without introducing pronounced rearrangements to the atomic topology. The structural and chemical flexibility is a consequence of the ability of

the corner-sharing tetrahedral chains running along the *c* axis to rigidly stretch or compress by simple rotation of the individual tetrahedra without affecting the tetrahedral bond lengths.

A well-constrained correlation between chemical composition, crystal structure and elastic properties is extremely important for the modeling of the behavior of pyroxenes in the Earth's interior. To this end the study of the high-temperature and high-pressure behavior of pyroxene end-members is necessary for constraining the effect of cation substitution at the M1 and M2 octahedra. In the present work we report results from diffraction experiments on the Fe end-member, $Fe_2Si_2O_6$. Three polymorphs of synthetic Fs_{100} have been observed at ambient conditions, namely orthoferrosilite (OFs, *Pbca*), clinoferrosilite (CFs, $P2_1/c$), and Fs-III (Lindsley et al., 1964). Subsequent structural investigation of these polymorphs demonstated that Fs-III (*P*-1) has a pyroxenoid structure (Weber, 1983). At room temperature pure OFs converts into a *C*2/*c* phase at 4.2 GPa through a reconstructive transition (Hugh-Jones et al., 1996) while a natural OFs_{82} follows two metastable transitions: first, above 10.1(1) GPa, to the monoclinic $P2_1/c$ phase (β-opx), and then, above 12.3(1) GPa, to a high pressure orthorhombic phase *Pbca* (γ-opx) (Dera et al., 2013). CFs transforms into a *C*2/*c* phase between 1.48 and 1.75 GPa with a volume decrease of 3% (Hugh-Jones et al., 1994). Here we report on a further single-crystal X-ray diffraction investigation of the compressional behavior of clinoferrosilite up to 45 GPa and thermal stability of laser-heated high-pressure pyroxenes.

Experimental

Single crystals of clinoferrosilite were synthesized at 9.5 GPa and 1100 °C using a split-sphere type multi-anvil apparatus at the Bayerisches Geoinstitut (Bayreuth, Germany) (BGI). The synthesis details are reported by Ismailova et al. (2015). The chemical composition was characterized using wavelength dispersive X-ray (WDX) microprobe analysis (JEOL JXA-8200; focused beam; accelerating voltage of 15 keV and beam current of 15 nA). Metallic Fe and

quartz were used as standards for Fe and Si, respectively. Atomic number effects, absorption, and fluorescence (ZAF) corrections were taken into account. The composition of clinoferrosilite (in wt% with standard deviations given in parentheses) was obtained by averaging 30 microprobe analyses: SiO_2 46.22(17), FeO 52.43(17), total 97.91(54), which led to a chemical formula $Fe_{1.93(3)}Si_{2.03(3)}O_6$ on the basis of 6 oxygen atoms.

Three separate in situ high-pressure single-crystal diffraction experiments were performed at the experimental stations P02.2 at Petra III (experiment **1** and **3**) and ID09 at the European Synchrotron Radiation Facility (experiment **2**). Diamond anvil cells produced at the BGI (Kantor et al., 2012) were used for pressure generation. Diamonds with culet diameters of 250 μm were glued on tungsten backing seats with an opening angle of 40° and aligned. Rhenium gaskets were indented to about 30 μm and subsequently drilled to obtain sample chambers with approximate diameters of 125 μm. Ferrosilite crystals with approximate size of 10×10×7 μm were selected by means of a three-circle Bruker diffractometer equipped with a SMART APEX CCD detector and a high-brilliance Rigaku rotating anode (Rotor Flex FR-D, Mo-Kα radiation). Ferrosilite crystals of proper quality were placed inside the sample chambers along with ruby spheres with diameter of about 10 μm. Au foil (thickness up to 5 μm; exp. **1**, **2**) or tungsten crystal (12×12×7; exp. **3**) were loaded together with the CFs crystals. To achieve quasi-hydrostatic conditions, the DACs were loaded with a neon pressure-transmitting medium using the in-house high-pressure gas loading system (Kurnosov et al., 2008). Pressures (Table 1) were determined using gold (for the points below the neon crystallization pressure) and neon equations of state (Fei et al. 2007) for experiment **1** and ruby fluorescence (Mao et al. 1986) for experiments **2** and **3**.

Monochromatic X-ray diffraction experiments were performed at the ESRF using X-rays with wavelength of 0.41505 Å and at Petra III with a wavelength of 0.2905 Å. The X-ray beam was focused to less than 10×10 μm by spherical mirror and bent Si(111) Laue monochromator at ESRF (Merlini and Hafland, 2013) and by Kirkpatrick-Baez mirrors at Petra III (Liermann et al.,

2015) . Diffraction patterns were collected using a MAR555 flat panel detector at ID09 (exp.**2**), a Perkin Elmer detector (exp. **3**) and a Pilatus 300K detector (exp. **1**) at P02.2. Before each experiment the detector-sample distance was calibrated with a LaB_6 standard using the procedure implemented in the program FIT2D (Hammersley et al., 1996). At each pressure both a wide-scan and a stepped ω-scan were collected for each crystal. Wide-scans consisted of exposure during rotations of ±20° of the DAC. Step scans consisted of individual exposures taken over 0.5° intervals to constrain the ω angle of maximum intensity of each peak. Collected diffraction images were analyzed using the program CrysAlis Pro© (Agilent, 2012).

The SHELXL program package was used for all structural determinations (Sheldrick, 2008). The structure models for $P2_1/c$ and $C2/c$ ferrosilite phases (Hugh-Jones et al. 1994) were used as starting parameters for the structural refinements at low pressure, whereas the crystal structure of the high-pressure $P2_1/c$ phase (HP-$P2_1/c$) observed above 30 GPa was solved using direct methods. The crystal structures were refined at 15 pressure points with isotropic displacement parameters. CIF files for all pressure points are attached to Supplementary materials.

The thermal stability of the HP-$P2_1/c$ clinoferrosilite was studied at the ID09 beamline in the course of experiment **2** using a double-side laser heating system (Kupenko et al., 2012). The crystal inside the DAC was laser-heated at 2200(100) K and at 46.3(1) GPa for ~10 minutes. Wide scans collected for the crystals before and after the heating were analysed using the program Dioptas (Prescher and Prakapenka, 2015).

Results

Equation of state and axial compressibilities of CFs

The performed X-ray diffraction experiments up to 45 GPa revealed the occurrence of two phase transitions of clinoferrosilite. The evolution with pressure of the unit-cell parameters (Table 1) is shown in Figure 2. The $P2_1/c \rightarrow C2/c$ transition occurs between 1.3(1) and 3.0(1) GPa, in agreement with previous observations of Hugh-Jones et al. (1994) who reported a transition pressure between 1.48(3) and 1.75(3) GPa. The phase transition results in a sudden decrease of all unit cell parameters. Contraction of the *a* and *c* axes is well pronounced while the *b* axis decreases only slightly. The resulting volume discontinuity is ~ 3% (Hugh-Jones et al., 1994) showing that the transition is first order in character. Upon further compression all the unit-cell parameters decrease continuously. However, a sudden change is observed between 30.0(1) and 35.9(1) GPa suggesting the occurrence of a second phase transition. At these pressures, the *b* and *c* axes decrease while *a* and *a*sinβ increase. This first-order transition is accompanied by a 5% decrease in volume. The evolution of the unit-cell parameters was followed up to 45 GPa in order to constrain their anisotropic compression.

The obtained *P*-*V* data (Table 1) were used to determine the equations of state of the *C*2/*c* and HP-$P2_1/c$ phases. The fitting was performed using the EOSFIT program (Angel et al., 2014). A third-order Birch-Murnaghan equation of state (EoS) was used for the *C*2/*c* phase. The initial volume V_0, room temperature isothermal bulk modulus K_{T0} and its pressure first pressure derivative K'_0 were determined (Table 2). The third-order truncation of the Birch-Murnaghan EoS, has been chosen based on the "normalized stress" defined as $F_E = P/3 f_E (1+2 f_E)^{5/2}$ (Angel, 2000) versus Eulerian finite strain f_E {($f_E = [(V_0/V)^{2/3}-1]/2$)}. For the *C*2/*c* phase, the F_E- f_E plot shows that the data are distributed along an inclined straight line (Fig. 3). From the intercept and slope of such linear fitting, we obtain K_{T0}=113(2) and K'_0=6.1 GPa, in good agreement with the *P*-*V* data fit.

For the high-pressure $P2_1/c$ phase the available four pressure points were insufficient to properly constrain an equation of state. The following procedure was, therefore, applied to enable the comparison of $Fe_2Si_2O_6$ compressibilities before and after the $C2/c \rightarrow$HP-$P2_1/c$ phase transition. The pressure point at 35.9 GPa was chosen as reference for HP-$P2_1/c$ phase. The values of the unit-cell volume, V_{36}, and of the bulk modulus, K_{36} were thus determined at 35.9 GPa by fitting a second-order BM EoS. The equation of state determined for $C2/c$ phase was then extrapolated up to 35.9 GPa by means of the EOSFITCalc program (Angel et al., 2014). The obtained parameters of the two $Fe_2Si_2O_6$ phases at 36 GPa are compared in Table 2. The significant decrease of bulk moduli after the phase transition indicates that at 36 GPa the HP-$P2_1/c$ phase is more compressible than the $C2/c$ phase.

The evolution of the individual unit-cell parameters of the $C2/c$ phase as a function of pressure was fit using a second- or third-order linearized Birch-Murnanghan EoS using the EOSFIT program (Angel et al, 2014). The cube of the lattice parameter was substituted for the volume in the EoS. To obtain the variation of β angles with pressure, the EoS fit of the $a\sin\beta$ parameter was divided by the corresponding EoS fit of the unit-cell parameter a. The choice of EoS order was made on the base of F_E-f_E plots calculated for the unit cell constants. F_E-f_E data points for a and $a\sin\beta$ lie on inclined straight lines so that a third-order Birch-Murnanghan EoS was applied for fitting the P-a and P-$a\sin\beta$ data. The F_E-f_E data points for the b and c axes are distributed along horizontal lines, therefore a second-order EoS was used (Table 2).

The obtained EoS parameters values (Table 2) reflect a strong compressional anisotropy of the $C2/c$ phase. The normalized unit-cell parameters calculated as X_P/X_0 (X_P = experimentally determined parameters a, $a\sin\beta$, b, c at pressure point P; X_0 = EoS values at ambient pressure) are shown in Figure 4. The $a\sin\beta$ is the stiffest direction over the whole pressure range. The c axis is the second stiffest direction at least up to ~15 GPa. At higher pressures a crossover is observed and the c axis becomes more compressible than the a axis. The b axis is the softest direction. Therefore the $C2/c$ phase follows the characteristic scheme of clinopyroxenes

180 $\beta_b > \beta_c \approx \beta_a > \beta_{asin\beta}$ (Angel and Hugh-Jones, 1994; Nestola et al., 2004; Tribaudino et al., 2001; Hu
181 et al., 2015)

182 The individual unit cell parameters of the HP-$P2_1/c$ phase also have been fitted using
183 linearized second-order Brich-Murnanghan EoS, with a reference pressure of 35.9 GPa (Table
184 2). As a result of the phase transformation the *a, a*sinβ and *b* directions become softer than in
185 $C2/c$ phase while the *c* direction appears to be significantly stiffer. Thus, the HP-$P2_1/c$ phase
186 follows the scheme $\beta_b > \beta_a \approx \beta_{asin\beta} > \beta_c$. The different anisotropy with respect to that of the $C2/c$
187 phase indicates that the HP-$P2_1/c$ phase possesses a different mechanism to accommodate
188 pressure changes.

189

190 **High-pressure structural behavior of clinoferrosilite**

191

192 Structural data were obtained for clinoferrosilite at 15 pressure points from ambient conditions
193 up to 45 GPa (Table 1, Figure 2). Results of the structural refinements are given in CIFs in
194 Supplementary Information. The $P2_1/c \rightarrow C2/c$ transition detected in the present study between
195 1.3 and 3.0 GPa has been described in detail by Hugh-Jones et al. (1994) whose study was
196 limited, however, in their study to 4.3 GPa. Here we address the high-pressure evolution of the
197 $C2/c$ phase up to 30 GPa and its transformation into the HP-$P2_1/c$ phase.

198 The crystal structure of the $C2/c$ phase is based on three crystallographically distinct
199 polyhedra: two octahedra, $Fe1O_6$ and $Fe2O_6$, and one tetrahedron, SiO_4 (Fig. 1). The Si1 site is
200 bonded to four oxygen atoms: O1, O2, O3A and O3B. The tetrahedra are connected via bridging
201 O3 atoms to form chains running along the *c* axis. At 3 GPa the O3-O3-O3 angle is 137.54°
202 indicating that the chain possesses strongly rotated O-configuration (Thompson, 1970). The SiO_4
203 tetrahedra are distorted: the Si1-O bond distances are distributed between 1.59 and 1.66 Å with
204 the Si1-O3 bond being the longest one (Fig. 5). The quadratic elongation and angular variation
205 parameters (Robinson et al., 1971) have been used to determine the non-ideality of the

coordination polyhedra. For the SiO_4 tetrahedra, the quadratic elongation and angular variation are 1.0032 and 13.30˚ at 3 GPa, respectively. The Fe1 atom at the M1 site forms three pairs of symmetry equivalent bonds with the oxygen atoms: Fe1-O1A, Fe1-O1B and Fe1-O2. The M1 octahedra share a common O1B–O1B edge, forming dense chains parallel to the *c* direction. The Fe-O1B bond is the longest one, while the Fe1-O1A and Fe1-O2 have nearly the same length (Fig.6a). The quadratic elongation and angular variation for $Fe1O_6$ octahedra are 1.0075 and 25.30˚, respectively. The Fe2 atom at the M2 site occupies the space between the tetrahedral chains and the chains of $Fe1O_6$ octahedra. The three pairs of symmetry equivalent oxygen atoms O1, O2, O3A are located in the first coordination sphere of the Fe2 atom. Two O3B atoms that fall into coordination of the $M2^{[VIII]}$ site in Ca-rich pyroxenes are also shown in Figure 6b although at 3 GPa the Fe2-O3B bond lengths are larger than 3 Å. The $Fe2O_6$ octahedra are more distorted with respect to the $Fe1O_6$, as a consequence the quadratic elongation and angular variation for the $Fe2O_6$ octahedra are larger, i.e. 1.0167 and 28.89˚, respectively.

With increasing pressure all structural units undergo an anisotropic distortion. The evolution of volumes and selected bonds distances of $Fe1O_6$, $Fe2O_6$ and SiO_4 polyhedra is shown in Figs. 5-7. The polyhedral compressibilities have been obtained by fitting a second-order Birch-Murnaghan equation of state to the polyhedral volumes, and a linearized BM2 EoS to the bond lengths.

Between 3 and 30 GPa, the volume of the $Fe1O_6$ octahedra decreases from 12.58 to 10.89 $Å^3$ with a bulk modulus of 130(8) GPa (Fig. 7a). The evolution of the individual Fe1-O bonds are anisotropic (Fig. 6a) with a compressibility scheme β(Fe1-O1B) = 4.26 x 10^{-3} GPa^{-1} > β(Fe1-O2) = 3.09 x 10^{-3} GPa^{-1} >> β(Fe1-O1A) = 1.49 x 10^{-3} GPa^{-1}. As a result, the $Fe1O_6$ octahedron becomes more regular with pressure and, at 30 GPa, its quadratic elongation and angle variance decrease to the values of 1.0031 and 10.40°, respectively.

The $Fe2O_6$ octahedron is much softer than the $Fe1O_6$ octahedron. Between 3 and 30 GPa, the volume of $Fe2O_6$ decreases from 13.58 to 11.33 $Å^3$ and its bulk modulus is 90(5) GPa (Fig.

7a). As expected, the longest Fe2-O bonds are more compressible than the shorter (Fig. 6b) with the following compressibility scheme: β(Fe2-O3A) = 13.89 x 10^{-3} GPa^{-1}>> β(Fe2-O1) = 2.40 x 10^{-3} GPa^{-1}> β(Fe2-O2) = 0.53 x 10^{-3} GPa^{-1}. The significant compression of the Fe2-O3A bonds result in a much less distorted $Fe2O_6$ octahedron at 30 GPa having a quadratic elongation and an angle variance of 1.0078 and 23.61°, respectively. Note also that the distance from Fe2 to the O3B oxygen which is part of the coordination polyhedra of *C*2/*c* pyroxenes having large cations as Ca and Na at the M2 site, is still larger than 3 Å at 30 GPa and therefore up to this pressure Fe2 remains six-fold coordinated.

As anticipated, the tetrahedron $Si1O_4$ is the most rigid structural unit of the pyroxene structure. Between 3 and 30 GPa, its volume decreases from 2.226 to 2.104 $Å^3$ with a bulk modulus of 360(21) GPa (Fig. 7b). The Si1-O2, Si1-O1 and Si1-O3B bonds (Fig. 5) show compressibilities of 1.14 x 10^{-3}, 1.04 x10^{-3} and 0.94x10^{-3} GPa^{-1}, respectively. The Si-O3A bond is slightly less compressible (β=0.70x10^{-3} GPa^{-1}). The major change associated with the tetrahedral chains is the continuous increase in kinking, identified by the decrease of the O3-O3-O3 angle which reaches the value of 133.5° at 30 GPa.

*C*2/*c* to HP-*P*2$_1$/*c* phase transformation

Between 30 and 35.8 GPa, CFs undergoes a first-order phase transformation to a HP-*P*2$_1$/*c* phase. The lowering of the symmetry is due to the rearrangement of half of the layers of corner-sharing SiO_4 tetrahedral chains in which the Si atoms become octahedrally coordinated. This forms a new type of layer by polymerization of $Si2O_6$ polyhedra via common edges (Fig. 8). The remaining Si chains (Si1) retain their tetrahedral coordination.

The HP-*P*2$_1$/*c* clinoferrosilite phase is isostructural with β-diopside observed above 50 GPa by Plonka et al. (2012). As in the case of β-diopside, the octahedral coordination of the Si2 atom is a result of its displacement from the tetrahedral position in the *C*2/*c* phase to a new site

directly above the Fe1 atoms. This displacive transformation leads to increase of the Si coordination, with consequent increase of the Si2-O bond distances and polyhedral volume. Moreover, the face-sharing configurations of the $Si2O_6$ and $Fe1O_6$ octahedra leads to significant distortion of these polyhedral, resulting in octahedral angle variance values of 57.23 and 101.80, respectively. The larger distortion of the $Fe1O_6$ octahedra is mainly due to three bond distances Fe1-O4B, Fe1-O4A and Fe1-O5, which are much larger than the Fe1-O bonds of the *C*2/*c* CFs structure at 30 GPa (Fig. 6a). As a result, the $Fe1O_6$ volume increases slightly at the transition (Fig. 7a). In contrast to $Fe1O_6$, the $Fe2O_6$ octahedron undergoes a less severe distortion due to the phase transformation. The six Fe2-O bonds lengths are much more similar, with some of them only slightly larger than the Fe2-O distances in the *C*2/*c* phase at 30 GPa (Fig. 6b), as a consequence, the resulting octahedral volume of $Fe2O_6$ increases only slightly at the transition (Fig. 7a). It is also worth noting that one of the two equivalent Fe2-O3B bond distances, which were larger than 3 Å (Fig. 6b) in the *C*2/*c* phase, is much shorter in the HP-$P2_1/c$ phase (2.88 Å). This suggests that the coordination number of Fe2 site in the HP-$P2_1/c$ phase should then be considered as 6 + 1.

In contrast, the $Si1O_4$ tetrahedral volume decreases at the transition (Fig. 7b), while increasing its distortion. Accordingly, angle variance and quadratic elongation increase to 24.98° and 1.0167. The phase transition is accompanied by pronounced kinking of the tetrahedral chains indicated by the decrease of the O3-O3-O3 angle to 128.7˚.

The transformation to the HP-$P2_1/c$ phase is accompanied by the appearance of diffuse scattering along the a^* direction. This increases with pressure with consequent deterioration of the quality of the diffraction data preventing meaningful structure refinements above 45 GPa. Streaking of the diffraction spots along the a^* axis has been observed in high-pressure phase transition of pyroxenes and it is believed to be induced by appearance of stacking faults aligned along the (100) direction (Hugh-Jones et al., 1996; Finkelstein et al., 2015).

Thermal stability of the *C*2/*c* clinoferrosilite phase

The laser heating experiment of the HP-$P2_1/c$ phase showed that at 46.3(1) GPa it decomposes into stishovite and wüstite after heating up to 2200K. The unit cell parameters of the HP-$P2_1/c$ crystal at 46.3(1) GPa and room temperature are: a = 9.16(3) Å, b = 7.906(4) Å, c = 4.59(2) Å, β = 98.7(5)°, and V = 328(2) Å^3. The wide scan collected after heating revealed the appearance of powder rings instead of reflections belonging to the HP-$P2_1/c$ single crystal. The d-spacings of such powder rings corresponded to those of stishovite and wüstite calculated at 46.3(1) GPa using the equations of state of Andrault et al. (2003) and Fischer et al. (2011), respectively.

Discussion

Pyroxenes belonging to the quadriteral enstatite ($Mg_2Si_2O_6$)-ferrosilite ($Fe_2Si_2O_6$)-diopside ($CaMgSi_2O_6$) - hedenbergite ($CaFeSi_2O_6$) are among the most abundant minerals in the Earth's upper mantle and therefore play an important role in determining the physical and chemical properties of this region. The *C*2/*c* pyroxene polymorphs are likely to be the most relevant under upper mantle conditions (Hugh-Jones et al., 1996; Woodland, 1998). Several studies have been focused on chemically different clinopyroxenes to constrain the effect of Mg-Fe substitution at the M1 site and of Ca-Fe-Mg substitution at the M2 site on the compressibility of diopside (Di, $CaMgSi_2O_6$, studied up to 10 GPa, Zhang et al., 1997), hedenbergite (Hd, $CaFe_{0.67}Mn_{0.16}Mg_{0.17}Si_2O_6$, studied up to 33 GPa, Hu et al., 2015; $CaFeSi_2O_6$, studied up to 10 GPa, Zhang et al., 1997) and clinoferrosilite (present study up to 45 GPa). The evolution with pressure of the unit cell parameters of these clinopyroxenes is given in Figure 2.

The bulk moduli values of Di and Hd, 104.1(9) and 117(1) GPa respectively (Zhang et al. 1997), indicate that substitution of Fe^{2+} cations (r=0.92 Å) by smaller Mg^{2+} cations (r=0.86 Å) at

the M1 site causes softening of the *C*2/*c* structure. Such anomalous behavior was also observed for garnets, olivine (Zhang et al., 1997) and Fe-Mg spinel solid solutions (Hazen, 1993). Hazen (1993) suggested that the presence of edge-sharing (Mg^{2+}, Fe^{2+})O_6 octahedra with a short cation-cation distance gives rise to *d* electron repulsion across the shared edge explaining the relative incompressibility of Fe-rich silicates. The increased stiffness of Fe-bearing pyroxenes may explain their lower transition pressures in comparison with their Mg-analogous. For example the $P2_1/c \rightarrow C2/c$ transformation occurs between 1.5 and 1.8 GPa for clinoferrosilite (Hugh-Jones et al., 1994) and above 7 GPa for clinoenstatite (Angel and Hugh-Jones, 1994); the $Pbca \rightarrow P2_1/c$ transition in orthopyroxenes was observed above 10.1 GPa for orthoferrosilite, OFs_{82} (Dera et al., 2013) and at 14.6 GPa for orthoenstatite, En_{90} (Finkelstein et al., 2015). The $C2/c \rightarrow$ HP-$P2_1/c$ transition was observed for diopside, Di, above 54 GPa (Plonka et al., 2012) while no HP-$P2_1/c$ phase has been yet observed for hedenbergite, Hd, which has *C*2/*c* symmetry up to 33 GPa (Hu et al., 2015). However, the presence of Fe^{2+} at the M1 site may be expected to cause a phase transitions to the HP-$P2_1/c$ phase between 33 and below 54 GPa.

The cation occupancy at the M2 site also strongly influences the structural and compressibility trends. For example, the presence of more than 15% of Ca^{2+} in clinoenstatite results in an eight-fold coordination of the M2 site and stability of the *C*2/*c* phase at ambient conditions. Less than 15% Ca^{2+} gives rise to a decrease of the $P2_1/c \rightarrow C2/c$ transition pressure (Nestola et al., 2004). The compressibility of *C*2/*c* phases is likely to decrease with increasing Ca^{2+} content although the available data are limited to few pressure points below 9 GPa (Nestola et al., 2004; Angel and Hugh-Jones, 1994). The Ca^{2+} for Fe^{2+} substitution along the Fs-Hd is ambiguous due to the presence of Mg^{2+} and Mn^{2+} cations at the M1 site of natural Hd (Hu et al., 2015). The *C*2/*c* phases of Hd and Fs have bulk moduli values of 131(4) and 113(3) GPa whereas their pressure derivatives are 3.8(3) and 6.3(3) GPa, respectively. Thereby, CFs is softer than Hd at low pressures but stiffer above ~20 GPa due to the larger K' value.

335 The *C*2/*c* polymorphs of clinopyroxenes undergo compression according to the common
336 scheme $\beta_b>\beta_c\approx\beta_a>\beta_{asin\beta}$ with slight differences in compressibilities of *a* and *c* axes (Hu et al.,
337 2015, Zhang et al., 1997 and this study). The compression of the *C*2/*c* structures is largely
338 governed by rotation of rigid SiO_4 tetrahedra and compression of the MO_6 octahedra.

339 A different compression scheme, $\beta_b>\beta_a\approx\beta_{asin\beta}>\beta_c$, was found for the HP-$P2_1/c$
340 clinoferrosilite in the present study. The increase in compressibility of the *a* and *a*sinβ directions
341 is caused by the presence of face sharing $Fe1O_6$ and $Si2O_6$ octahedra and of long and relatively
342 soft (Fe, Si)-O4 and (Fe,Si)-O5 bonds (Fig. 5,6). The stiffness of the *c* axis may result firstly by
343 the loss of rotational freedom of half of tetrahedral layers present in *C*2/*c* phase because of their
344 transformation into layers of edge-sharing SiO_6 octahedra. The negligible change of O3-O3-O3
345 angle from 128.7 to 128.4˚ between 36 and 45 GPa of the $Si1O_4$ tetrahedral chains also indicates
346 that compression of tetrahedral rotation is suppressed in the HP-$P2_1/c$ structure. Moreover, the
347 repulsion of Fe^{2+} atoms in dense octahedral chains running along the *c* axis likely contributes to
348 the low compressibility of the HP-$P2_1/c$ structure in this direction. Interestingly, the high-
349 pressure phase of orthoenstatite (OEn_{90}) occurring above 40 GPa and also containing a layer of
350 six-coordinated silicon does not reveal the crossover in axial compressibilities (Finkelstein et al.,
351 2015). Up to 50 GPa the conventional scheme of compression $\beta_b>\beta_c>\beta_a$ is preserved. Likely the
352 presence of Mg^{2+} at the M1 site instead of Fe^{2+} does not prevent compression along the *c* axis.

353 The compressibility systematics of clinopyroxenes has been a subject of intensive research.
354 Several factors responsible for the bulk moduli variation have been proposed: *i.e.* volume-bulk
355 modulus systematic at ambient conditions (Bridgman, 1923), cation size and occupancy of the
356 M1 site (Thompson and Downs, 2004), type (sympathetic or antipathetic) of the M2-O3 bonds
357 (McCarthy et al., 2008). The theoretical models constructed on the basis of the available
358 compressibility data collected at relatively low-pressure often show discrepancies with new
359 experimental data collected at much higher pressures (Plonka et al., 2012). Undoubtedly, more
360 experiments on chemically different clinopyroxenes at pressures above 10 GPa are required to

obtain bulk moduli and their pressure derivatives values to describe realistically the pyroxene compression behavior at upper mantle conditions.

Implication

Recently, Finkelstein et al. (2015) has proposed a new family of high-pressure "post-pyroxene" structures that possess pyroxene-like M1 and M2 sites interleaved with sheets of Si cations in five- and six-fold coordination. Up to date this family is composed by three types of structures: α-post-clinopyroxene (α-pcpx, $P2_1/c$), α-post-orthopyroxene (α-popx, $Pca2_1$) and β-post-orthopyroxene (β-popx, $Pca2_1$) following the notation system of Finkelstein et al. (2015).

The α-pcpx phase of CFs observed above 30 GPa in the present study (denoted as HP-$P2_1/c$ phase) has two types of Si-O layers, an ilmenite-like layer composed of silicon octahedra and a conventional pyroxene layer with tetrahedral chains. An isostructural phase was detected for diopside above 53 GPa (Plonka et al., 2012) and denote as β-diopside. β-diopside possesses two additional Ca-O bonds to the bridging O3 atoms of the tetrahedral chains which are considerably less kinked (150.3° at 53 GPa) in comparison with HP-$P2_1/c$ phase (128.7° at 36 GPa). The eight-fold coordination of the M2 site is likely to be responsible for the larger transition pressure of $C2/c$ diopside. Longer M2-O bonds and more extended tetrahedral chains could provide the crystal structure with additional freedom for compression with respect to the $C2/c$ CFs phase.

The α-popx and β-popx were observed for orthoenstatite (En_{90}) at 29.9 GPa and 40.3 GPa, respectively (Finkelstein et al., 2015). The α-popx has one Si-O layer that is entirely tetrahedral and one layer that contains both tetrahedra and 4+1 coordinated Si in distorted square pyramids. The β-popx retains the mixed coordinated layer while the tetrahedral layer transforms to an ilmenite-like layer with silicon in octahedral coordination.

385 It has been proposed that in low-temperature subduction zones (T<1500 K) pyroxene may
386 survive as metastable phase through the wadsleyte+stishovite and ringwoodite+stishovite
387 stability fields and eventually directly transforms to the ilmenite structure (Hogrefe et al., 1994,
388 Mierlo et al., 2013, Agrusta et al., 2014; Serghiou et al., 2000). The metastable persistence of
389 pyroxene may therefore have a strong influence on the dynamics of cold subducting slabs. It
390 could cause slab deceleration and possibly transient stagnation in the transition zone. Moreover,
391 the significant density increase (16 %) associated with the pyroxene to ilmenite transition was
392 proposed to contribute to the origin of deep focus earthquakes (Hogrefe et al., 1994; Mierlo et
393 al., 2013). The discovery of post-pyroxene phases in pyroxene compression experiments
394 provides better constrain on the possible metastable phases of pyroxene (Plonka et al., 2012;
395 Finkelstein et al., 2015; present study), indicating that the pyroxene → ilmenite transformation
396 likely does not occur directly. The step-wise nature was also suggested by Tomioka (2007) who
397 proposed a model for the shear mechanism for the pyroxene to ilmenite transformation. This
398 mechanism is based on sweeping of partial dislocations that is accompanied by introduction of
399 stacking faults aligned parallel to (100). The observation of topotaxial intergrowth of akimotoite
400 and enstatite in a shocked chondritic meteorite (Tomioka and Fujino, 1997) as well as the
401 presence of diffuse scattering along the a^* direction in post-pyroxenes as observed in the present
402 study are in agreement with the proposed shear mechanism for the transformation. However, the
403 intermediate structure, expected by Tomioka (2007) to occur after the first gliding of the partial
404 dislocations, differs from the HP-$P2_1/c$ phase observed in the present study. In contrast to the
405 prediction, M1 and M2 atoms preserve typical for pyroxenes chain arrangement and do not form
406 honeycomb-like layer as well as half of silicon stays in tetrahedral coordination. Likely that at
407 least at room temperature the mechanism of transformation involves several steps and more
408 gradual as expected.

409 Despite the high relevancy of post-pyroxenes to the mineralogical assembly of cold
410 subducting slabs, there is no data on their thermal stability to the best of our knowledge. The

411 preliminary laser heating experiments presented in this study is a first step for elucidating the
412 behavior of post-pyroxenes under real geological conditions. The post-clinoferrosilite was found
413 to decompose after heating at 2200(100) K and 46.3(1) GPa. More detailed high-temperature
414 investigations on chemically different post-pyroxenes are required to better understand their
415 importance in geological environments.
416
417
418 **Acknowledgments**
419
420 The authors are grateful to A. Kurnosov for help with loading of the diamond anvil cells. AP
421 thanks the Deutsche Forschungsgemeinschaft (DFG) (Project No. BO 2550/8-1) for financial
422 support. Parts of this research were carried out at the light source PETRA III at DESY, a member
423 of the Helmholtz Association (HGF), and at the European Synchrotron Radiation Facility.
424

References

Agilent (2012). CrysAlis PRO. Agilent Technologies, Yarnton, Oxfordshire, England.

Agrusta, R., Hunen, J., and Goes, S. (2014) The effect of metastable pyroxene on the slab dynamics. Geophysical Research Letters, 41, 8800–8808.

Akashi, A., Nishihara, Y., Takahashi, E., Nakajima, Y., Tange, Y., and Funakoshi, K. (2009) Orthoenstatite/clinoenstatite phase transformation in $MgSiO_3$ at high-pressure and high-temperature determined by in situ X-ray diffraction: Implications for nature of the X discontinuity. Journal of Geophysical Research: Solid Earth, 114, B04206.

Andrault, D., Angel, R.J., Mosenfelder, J.L., and LeBihan, T. (2003) Equation of state of stishovite to lower mantle pressures. American Mineralogist, 88, 301–307.

Angel, R.J. (2000) Equations of State. Reviews in Mineralogy and Geochemistry, 41, 35-59,

Angel, R.J, Gonzalez-Platas, J., and Alvaro, M. (2014) EosFit-7c and a Fortran module (library) for equation of state calculations. Zeitschrift für Kristallographie, 229, 405-419.

Angel, R.J., and Hugh-Jones, D.A. (1994) Equations of state and thermodynamic properties of enstatite pyroxenes. Journal of Geophysical Research: Solid Earth, 99, B10, 19777-19783.

Bridgman, P.W. (1923) The compressibility of thirty metals as a function of pressure and temperature. Proceedings of the American Academy of Arts and Sciences, 58, 165–242.

Dera, P., Finkelstein, G.J., Duffy, T.S., Downs, R.T., Meng Y., Prakapenka V., and Tkachev S. (2013) Metastable high-pressure transformations of orthoferrosilite Fs_{82}. Physics of the Earth and Planetary Interiors, 221, 15-21.

Deuss, A., and Woodhouse, J.H. (2002) A systematic search for mantle discontinuities using SS-precursors. Geophysical Research Letters, 29, 8, 90-1–90-4.

Ferot, A., and Bolfan-Casanova, N. (2012) Water storage capacity in olivine and pyroxene to 14 GPa: Implications for the water content of the Earth's upper mantle and nature of seismic discontinuities. Earth and Planetary Science Letters, 349-350, 218–230.

Fei, Y., Ricolleau A., Frank, M., Mibe, K., Shen, G., and Prakapenka, V. (2007) Toward an internally consistent pressure scale. Proceedings of the National Academy of Sciences, 104, 9182-9186.

Finkelstein, G.J., Dera, P.K., and Duffy, T.S. (2015) Phase transitions in orthopyroxene (En_{90}) to 49 GPa from single-crystal X-ray diffraction. Physics of the Earth and Planetary Interiors, 244, 78–86.

Fischer, R. A., Campbell, A. J., Shofner, G. A., Lord, O. T., Dera, P., and Prakapenka, V. B. (2011) Equation of state and phase diagram of FeO. Earth Planetary Science Letters, 304, 496-502.

Frost, D.J. (2008) The upper mantle and transition zone. Elements, 4, 171–176.

Hammersley, A.P., Svensson, S.O., Hanfland, M., Fitch, A.N., and Hausermann, D. (1996) Two-dimensional detector software: From real detector to idealised image or two-theta scan. High Pressure Research, 14, 235–248.

Hazen, R.M. (1993) Comparative compressibilities of silicate spinels: Anomalous behavior of $(Mg,Fe)_2SiO_4$. Science, 259, 206-209.

Hogrefe, A., Rubie, D. C., Sharp, T. G., and Seifert, F. (1994) Metastability of enstatite in deep subducting lithosphere. Nature, 372(6504), 351-353.

Hu, Y., Dera, P., and Zhuravlev, K. (2015) Single-crystal X-ray diffraction and Raman spectroscopy of hedenbergite up to 33 GPa. Physics and Chemistry of Minerals, 42, 595–608.

Hugh-Jones, D.A., Woodland, A.B., and Angel, R.J. (1994) The structure of high-pressure *C*2/*c* ferrosilite and crystal chemistry of high-pressure *C*2/*c* pyroxenes. American Mineralogist, 79, 1032-1041.

Hugh-Jones, D.A., Sharp, T.G., A.B., Angel, R.J., and Woodland, A.B. (1994) The transition of orthoferrosilite to high-pressure *C*2/*c* clinoferrosilite at ambient temperature. European Journal of Mineralogy, 8, 1337-1345.

Hugh-Jones, D.A., and Angel, R.J. (1994) A compressional study of $MgSiO_3$ orthoenstatite to 8.5 GPa. American Mineralogist, 79, 405–410.

Ismailova, L., Bobrov, A., Bykov, M., Bykova, E., Cerantola, V., Kantor I., Kupenko, I., McCammon, C., Dyadkin, V., Chernyshov, D., Pascarelli, S., Chumakov, A., Dubrovinskaia, N., and Dubrovinsky, L. High-pressure synthesis of skiagite-majorite garnet and investigation of its crystal structure. American Mineralogist, 100, 2650–2654.

Jacobsen S.D., Liu Z., Ballaran T.B., Littlefield E.F., Ehm L., and Hemley R.J. (2010) Effect of H2O on upper mantle phase transitions in $MgSiO_3$: Is the depth of the seismic X-discontinuity an indicator of mantle water content? Physics of the Earth and Planetary Interiors, 183, 234-244.

Kantor, I., Prakapenka, V., Kantor, A., Dera, P., Kurnosov, A., Sinogeikin, S., Dubrovinskaia, N., and Dubrovinsky, L. (2012) BX90: A new diamond anvil cell design for X-ray diffraction and optical measurements. Review of Scientific Instruments, 83, 12, 125102.

Kupenko, I., Dubrovinsky, L., Dubrovinskaia, N., McCammon, C., Glazyrin, K., Bykova, E., Boffa Ballaran, T., Sinmyo, R., Chumakov, A.I., Potapkin, V., Kantor, A., Rüffer, R., Hanfland, M., Crichton, W., and Merlini, M. (2012) Portable double-sided laser-heating system for Mössbauer spectroscopy and X-ray diffraction experiments at synchrotron facilities with diamond anvil cells. Review of Scientific Instruments, 83, 124501.

Kurnosov, A., Kantor, I., Boffa-Ballaran, T., Lindhardt, S., Dubrovinsky, L., Kuznetsov, A., and Zehnder, B. H. (2008) A novel gas-loading system for mechanically closing of various types of diamond anvil cells. Review of Scientific Instruments, 79, 045110.

Liermann, H.-P., Konôpková, Z., Morgenroth, W., Glazyrin, K., Bednarcik, J., McBride, E. E., Petitgirard, S., Delitz, J. T., Wendt, M., Bican, Y., Ehnes, A., Schwark, I., Rothkirch, A., Tischer, M., Heuer, J., H. Schulte-Schrepping, Kracht T., and H. Franz. (2015) The Extreme Conditions Beamline P02.2 and the Extreme Conditions Science Infrastructure at PETRA III. Journal of Synchrotron Radiation, 22, 908-924.

Lindsley, D.H., Davis, B.T., and Macgregor, I.D. (1964) Ferrosilite ($FeSiO_3$): Synthesis at high pressures and temperatures. Science, 144, 73-74.

Ma, C., Tschaunerb, O., Becketta, J.R., Liu Y., Rossmana, G.R., Zhuravlev, K., Prakapenka, V., Dera, P., Taylor, L.A. (2015) Tissintite, $(Ca,Na,\square)AlSi_2O_6$, a highly-defective, shock-induced, high-pressure clinopyroxene in the Tissint martian meteorite. Earth and Planetary Science Letters, 422, 195-205.

Mao, H.K, Xu, J., and Bell, P.M. (1986) Calibration of the ruby pressure gauge to 800 kbar under quasi-hydrostatic conditions. Journal of Geophysical Research, 9, 4673-4676.

McCarthy, A.C., Downs, R.T., and Thompson, RM. (2008) Compressibility trends of the clinopyroxenes, and in situ high-pressure single-crystal X-ray diffraction study of jadeite. American Mineralogist, 93, 198–209.

McCormick T.C. (1986) Crystal-chemical aspects of nonstoichiometric pyroxenes. American Mineralogist, 71, 1434-1440.

Merlini, M., and Hafland, M. (2013) Single-crystal diffraction at megabar conditions by synchrotron radiation. High Pressure Research, 33, 511-522.

Mierlo, W. L., Langenhorst, F., Frost, D. J., and Rubie, D. C. (2013) Stagnation of subducting slabs in the transition zone due to slow diffusion in majoritic garnet. Nature Geoscience, 6, 400–403.

Morimoto, N., Fabries, J., Ferguson, A.K., Ginzburg, I.V., Ross, M., Seifeit, F.A., and Zussman, J. (1989). Nomenclature of pyroxenes. Canadian Mineralogist, 27, 143–156.

Nestola, F., Tribaudino, M., and Boffa Ballaran, T. (2004) High-pressure behavior, transformation and crystal structure of synthetic iron-free pigeonite. American Mineralogist, 89, 189-196.

Plonka, A.M, Dera, P., Irmen, P., Rivers, M.L., Ehm, L., and Parise, J.B. (2012) β-diopside, a new ultrahigh-pressure polymorph of $CaMgSi_2O_6$ with six-coordinated silicon. Geophysical Research Letters, 39, L24307.

Prescher, C., and Prakapenka, V. (2015) DIOPTAS: a program for reduction of two dimensional X-ray diffraction data and data exploration. High Pressure Research, 35, 223–230.

Ringwood, A. E. (1982) Phase transformations and differentiation in subducted lithosphere: Implications for mantle dynamics, basalt petrogenesis, and crustal evolution. The Journal of Geology, 90, 611-643.

Robinson, K., Gibbs, G.V., and Ribbe, P.H. (1971). Science, 172, 567-70.

Serghiou, G., Chopelas, A., and Boehler, R. (2000) Explanation of pressure-induced transformations in chain silicates based on their modular structures. Journal of Physics: Condensed Matter, 12, 8939–8952.

Sheldrick G.M. (2008) A short history of SHELX. Acta Crystallographica, A64, 112.

536 Stixrude L., and Lithgow-Bertelloni C. (2005) Mineralogy and elasticity of the oceanic upper
537 mantle: origin of the low-velocity zone. Journal of Geophysical Research: Solid Earth, 110,
538 B03204.

539 Tomioka M. (2007) A model for the shear mechanism in the enstatite-akimotoite phase
540 transition. Journal of Mineralogical and Petrological Sciences, 102, 226-232.

541 Thompson, Jr., J.B. (1970) Geometrical possibilities for amphibole structures: model
542 biopyriboles. American Mineralogist, 55, 292-293.

543 Thompson, R.M., and Downs, R.T. (2004) Model pyroxenes II: Structural variation as a function
544 of tetrahedral rotation. American Mineralogist, 89, 614–628.

545 Tribaudino, M., Prencipe, M., Nestola, F., and Hanfland, M. (2001) A $P2_1/c$-$C2/c$ high-pressure
546 phase transition in $Ca_{0.5}Mg_{1.5}Si_2O_6$ clinopyroxene. American Mineralogist, 86, 807-813.

547 Weber, H.P. (1983) Ferrosilite III, the high-temperature polymorph of $FeSiO_3$. Acta
548 Crystallographica, C39, 1-3.

549 Woodland A.B. (1998) The orthorhombic to high-P monoclinic phase transition in Mg-Fe
550 Pyroxenes: Can it produce a seismic discontinuity? Geophysical Research Letters, 25, 8, 1241–
551 1244.

552 Zhang, L., Ahsbahs, H., Hafner, S.S., and Kutoglu A. Single-crystal compression and crystal
553 structure of clinopyroxene up to 10 GPa. American Mineralogist,

554

555 **Table 1**. Unit cell parameters of clinoferrosilite determined from single crystal X-ray diffraction
556 data at different pressures

557

N	P, GPa	exp.	Sp.Gr.	*a*, Å	*b*, Å	*c*, Å	β, °	V, Å^3
1	0.0001	3	$P2_1/c$	9.7190(5)	9.0907(6)	5.2393(1)	108.445(4)	439.12(4)
2	1.3(1)	1	$P2_1/c$	9.674(2)	9.032(3)	5.2237(6)	108.26(2)	433.4(2)
3	3.0(1)	2	$C2/c$	9.5140(4)	8.9625(3)	4.99994(8)	102.694(3)	415.92(2)
4	4.3(1)	1	$C2/c$	9.483(4)	8.917(4)	4.9899(6)	102.54(2)	411.9(2)
5	7.2(1)	2	$C2/c$	9.4244(2)	8.8508(6)	4.94454(9)	101.837(2)	403.67(3)
6	10.1(1)	2	$C2/c$	9.3758(4)	8.786(1)	4.9159(2)	101.481(4)	396.87(6)
7	13.5(1)	1	$C2/c$	9.311(5)	8.699(6)	4.8937(7)	101.21(3)	388.8(3)
8	17.9(1)	2	$C2/c$	9.2640(2)	8.6423(6)	4.8481(1)	100.838(2)	381.23(3)
9	21.2(1)	2	$C2/c$	9.2294(5)	8.585(1)	4.8236(2)	100.656(4)	375.62(6)
10	24.6(1)	2	$C2/c$	9.2169(4)	8.500(1)	4.8090(2)	100.562(3)	370.37(5)
11	30.0(1)	2	$C2/c$	9.1489(7)	8.449(2)	4.7640(3)	100.377(6)	362.25(9)
12	35.9(1)	2	$P2_1/c$	9.18(3)	8.11(2)	4.602(2)	100.3(1)	337.2(6)
13	35.9(1)	3	$P2_1/c$	9.23(2)	8.07(2)	4.605(3)	100.4(2)	337.6(9)
14	39.8(1)	2	$P2_1/c$	9.145(2)	7.982(7)	4.596(2)	99.65(2)	330.8(3)
15	45.0(1)	2	$P2_1/c$	9.093(3)	7.891(8)	4.572(1)	99.31(2)	323.7(3)

558

559

560

561

562

563

564

565

566

567

568

569 **Table 2**. Coefficients obtained by fitting the Birch-Murnanghan EoS to the unit-cell constants of
570 clinoferrosilite

	***C*2/c**		***C*2/*c****	***P*2$_1$/*c*****
a_0 (Å)	9.604(7)	a_{36} (Å)	9.060	9.192(6)
$K_{T0,a}$ (GPa)	90(9)	$K_{T36,a}$ (GPa)	394	260(23)
K'_a	13(2)	K'_a	7.2	fixed at 4
b_0 (Å)	9.049(1)	b_{36} (Å)	8.375	8.088(1)
$K_{T0,b}$ (GPa)	97(1)	$K_{T36,b}$ (GPa)	227	120(13)
K'_b	fixed at 4	K'_b	3.4	fixed at 4
c_0 (Å)	5.036(2)	c_{36}(Å)	4.718	4.605(5)
$K_{T0,c}$ (GPa)	124(3)	$K_{T36,c}$ (GPa)	256	381(80)
K'_c	fixed at 4	K'_c	3.4	fixed at 4
$a\sin\beta_0$ (Å)	9.331(4)	$a\sin\beta_{36}$ (Å)	8.924	9.06(1)
$K_{T0,a\sin\beta}$ (GPa)	180(12)	$K_{T36,a\sin\beta}$ (GPa)	375	286(56)
$K'_{a\sin\beta}$	6(1)	$K'_{a\sin\beta}$	5.1	fixed at 4
V_0 (Å)	426.2(2)	V_{36} (Å)	345.8	336.8(8)
K_{T0} (GPa)	113(3)	K_{T36} (GPa)	308	205(22)
K'	6.3(3)	K'	5.1	fixed at 4

571 *parameters resulting from extrapolation of equations of state up to 35.9 GPa
572 **fitted parameters assuming 35.9 GPa as a zero pressure

Figure captions

1. (a) The crystal structure of *C*2/*c* ferrosilite phase at 3 GPa; (b) the configuration of O-rotated tetrahedral chain with O3-O3-O3 angle of 137.5˚. Octahedra $Fe1O_6$ and tetrahedra SiO_4 are given in blue and green, respectively. Fe2 atoms are presented as orange spheres.
2. The high-pressure evolution of unit cell parameters of clinoferrosilite in comparison with other clinopyroxenes.
3. Birch's normalized stress F_E versus the Eulerian strain f_E for clinoferrosilite *C*2/*c* phase.
4. Normalised unit cell parameters of *C*2/*c* phase of clinoferrosilite.
5. The evolution of Si-O bond distances in clinoferrosilite under compression. Errors are indicated by vertical bars.
6. High-pressure evolution of selected Fe-O bond distances in the crystal structure of ferrosilite. Errors larger than symbols are indicated by vertical bars.
7. Pressure dependences of $Fe1O_6$, $Fe2O_6$ and SiO_4 polyhedral volumes in ferrosilite.
8. (a) Crystal structure of HP-$P2_1/c$ phase of clinoferrosilite at 35.9 GPa; (b) the configuration of O-rotated tetrahedral chain with O3-O3-O3 angle of 128.7˚; (3) arrangement of $Si2O_6$ octahedra. $Fe1O_6$, $Si2O_6$ and tetrahedra SiO_4 are given in blue, yellow and green, respectively. Fe2 atoms are presented as orange spheres.

This is a preprint, the final version is subject to change, of the American Mineralogist (MSA)
Cite as Authors (Year) Title. American Mineralogist, in press.
(DOI will not work until issue is live.) DOI: http://dx.doi.org/10.2138/am-2017-5853

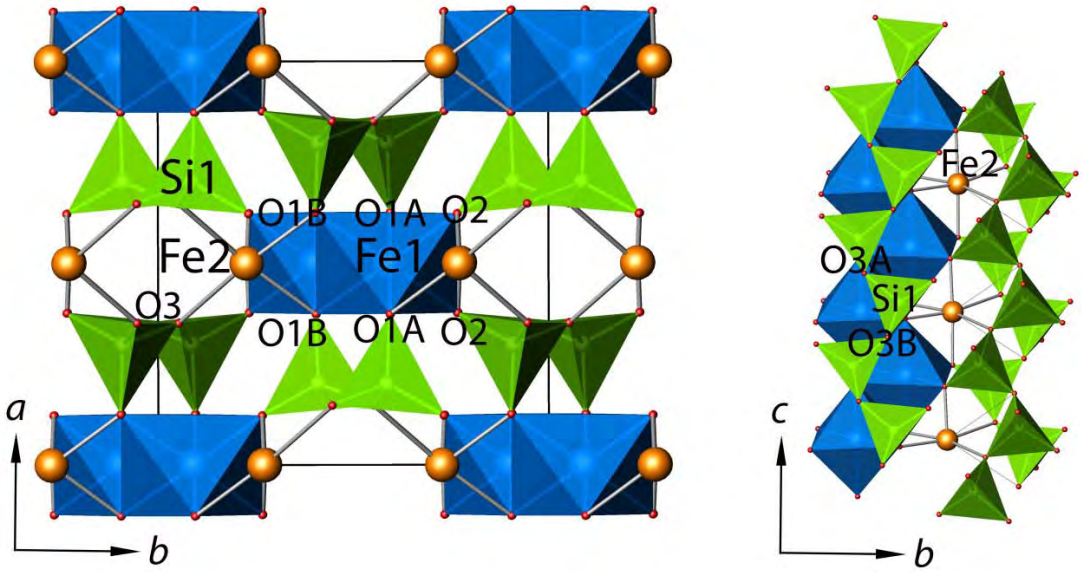

Figure 1. (a) The crystal structure of *C*2/*c* ferrosilite phase at 3 GPa; (b) the configuration of O-rotated tetrahedral chain with O3-O3-O3 angle of 137.5˚. Octahedra $Fe1O_6$ and tetrahedra SiO_4 are given in blue and green, respectively. Fe2 atoms are presented as orange spheres.

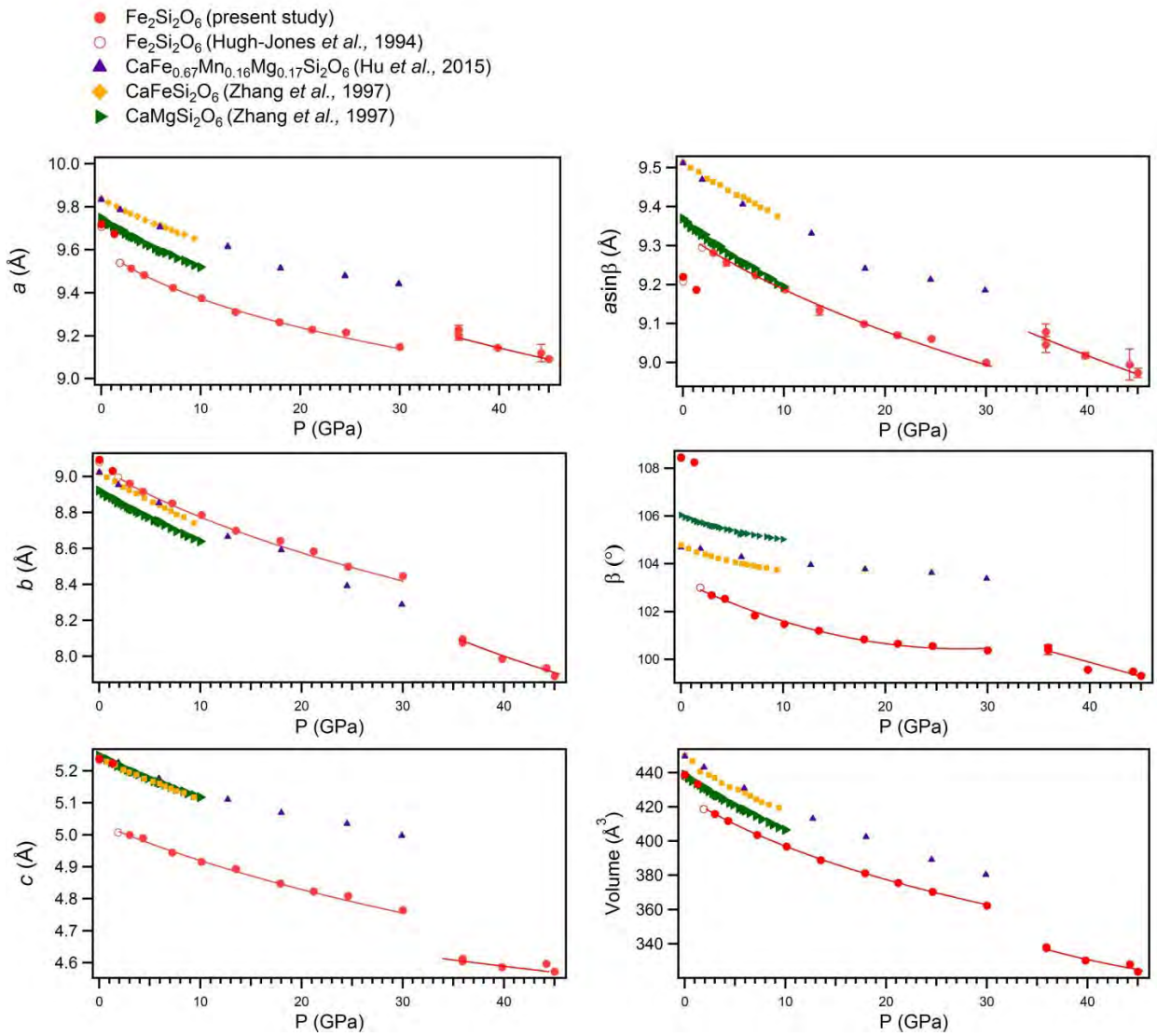

Figure 2. The high-pressure evolution of unit cell parameters of clinoferrosilite in comparison with other clinopyroxenes.

This is a preprint, the final version is subject to change, of the American Mineralogist (MSA)
Cite as Authors (Year) Title. American Mineralogist, in press.
(DOI will not work until issue is live.) DOI: http://dx.doi.org/10.2138/am-2017-5853

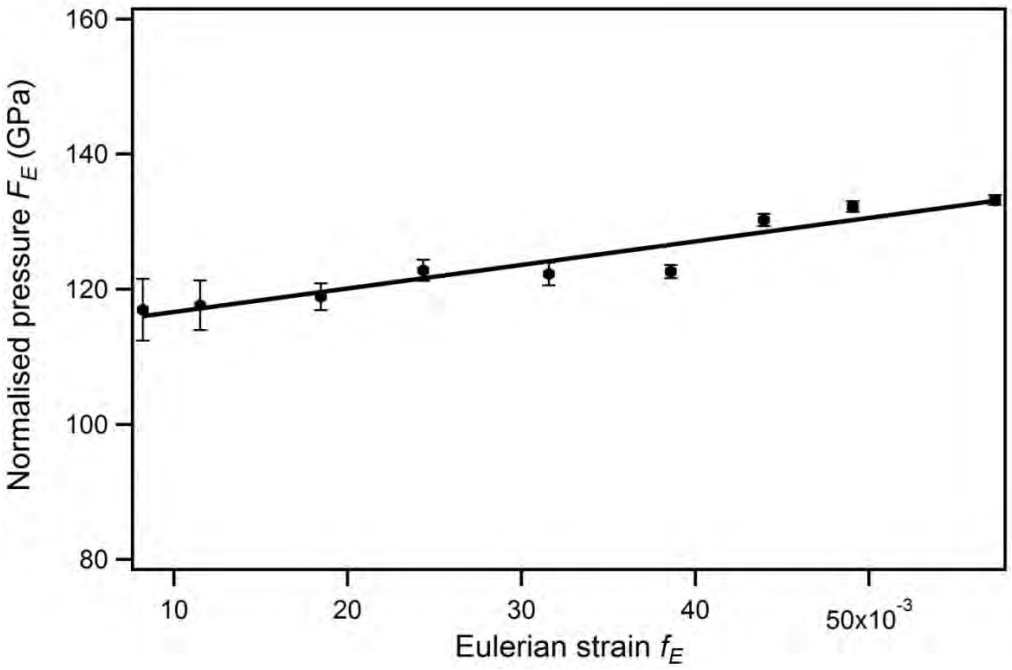

Figure 3. Birch's normalized stress F_E versus the Eulerian strain f_E for clinoferrosilite $C2/c$ phase.

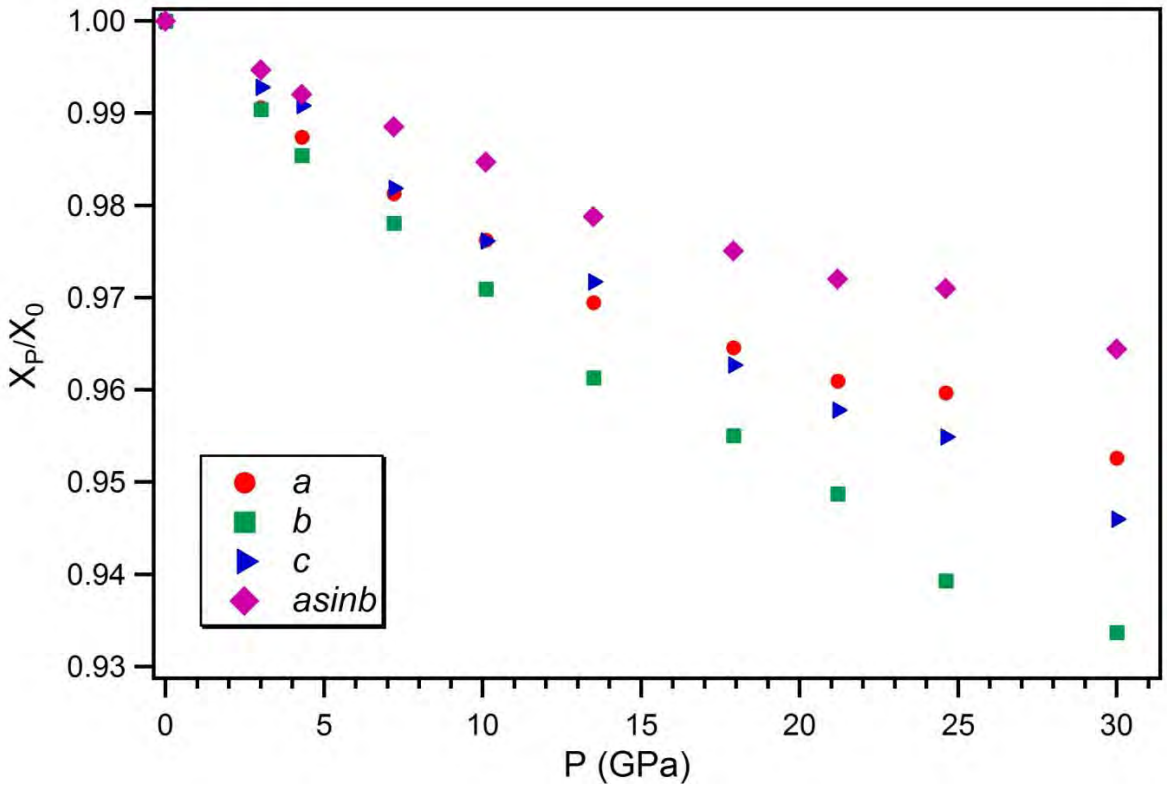

Figure 4. Normalised unit cell parameters of *C*2/*c* phase of clinoferrosilite

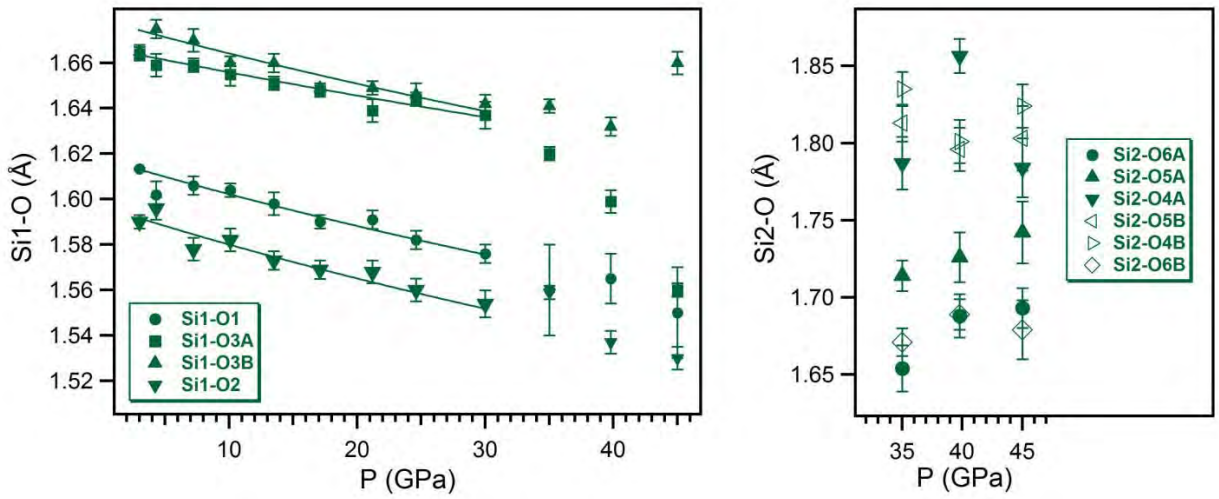

Figure 5. The evolution of Si-O bond distances in clinoferrosilite under compression. Errors are indicated by vertical bars.

This is a preprint, the final version is subject to change, of the American Mineralogist (MSA)
Cite as Authors (Year) Title. American Mineralogist, in press.
(DOI will not work until issue is live.) DOI: http://dx.doi.org/10.2138/am-2017-5853

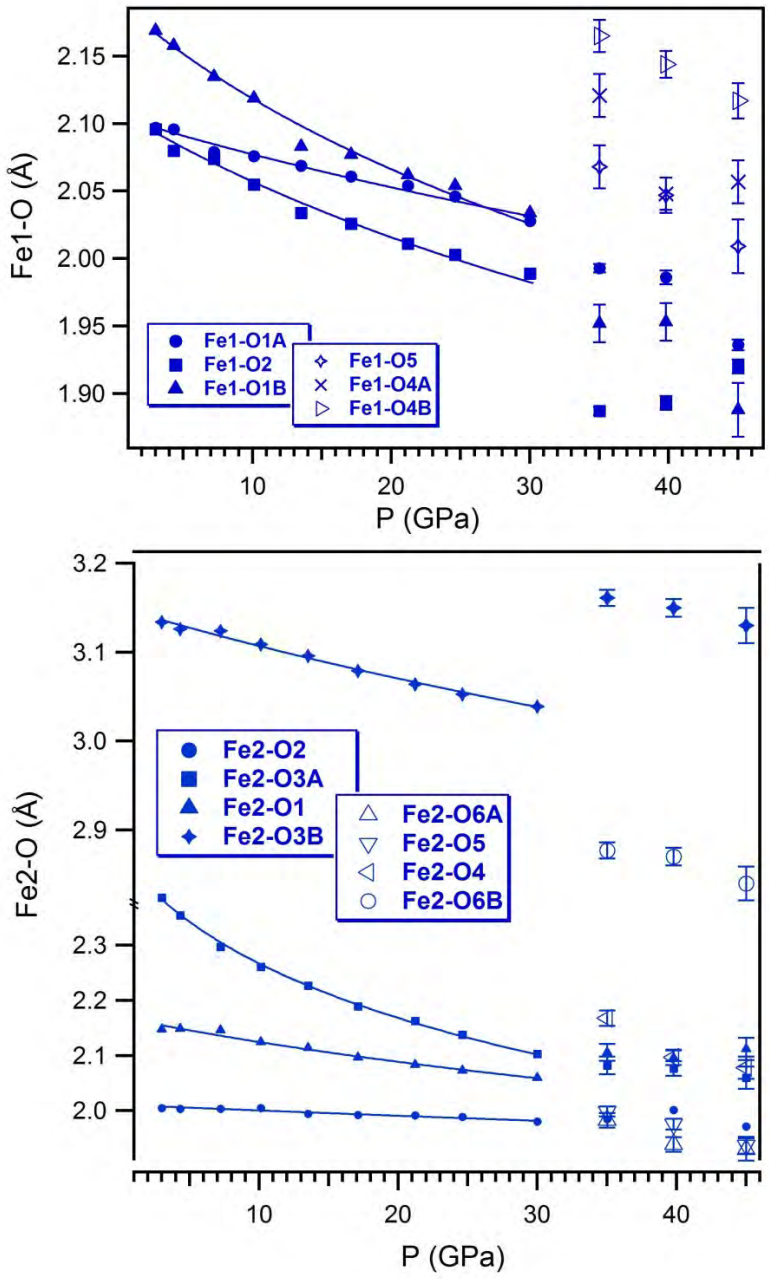

Figure 6. High-pressure evolution of selected Fe-O bond distances in the crystal structure of ferrosilite. Errors larger than symbols are indicated by vertical bars.

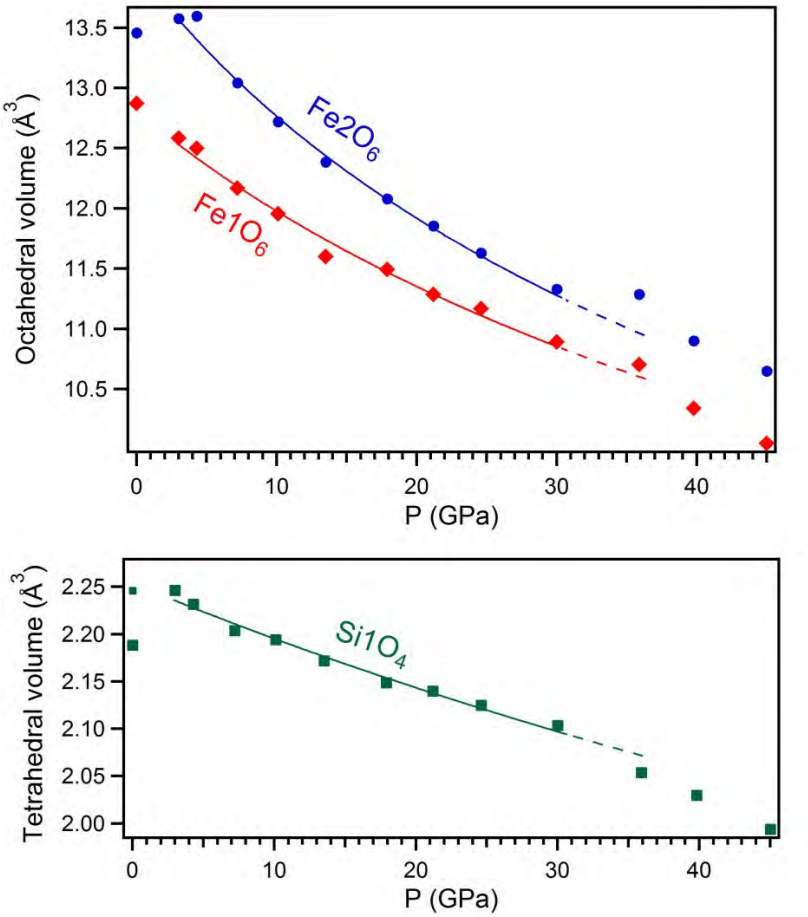

Figure 7. Pressure dependences of $Fe1O_6$, $Fe2O_6$ and SiO_4 polyhedral volumes in ferrosilite.

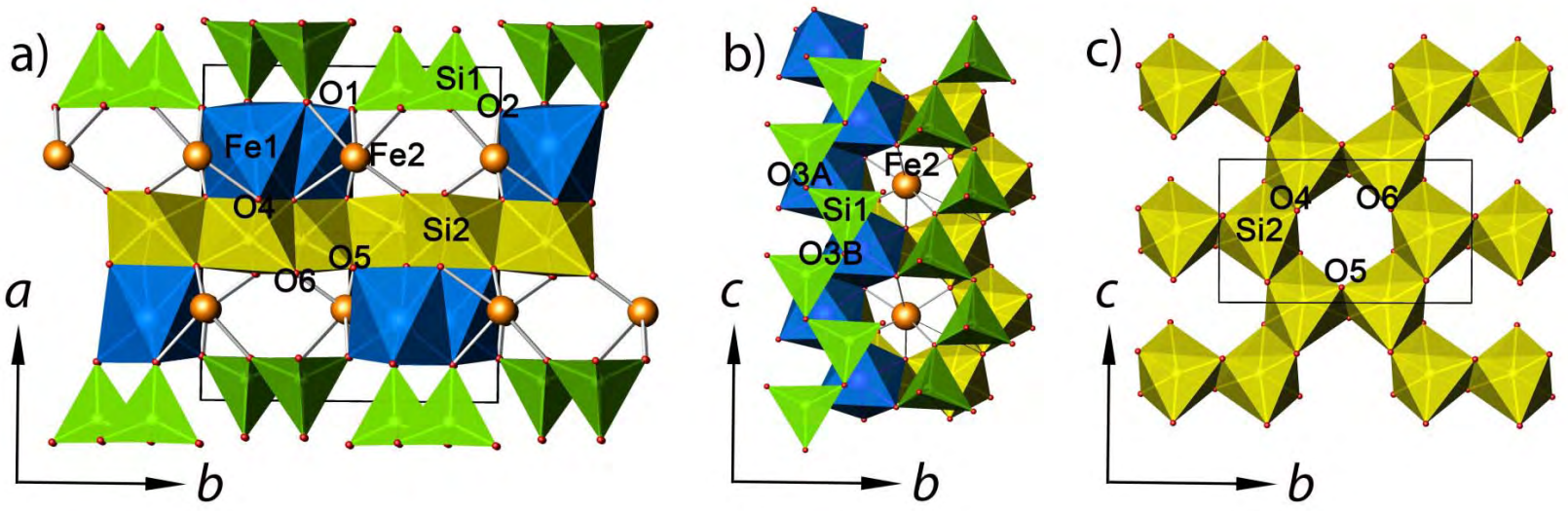

683

684 **Figure 8**. (a) Crystal structure of HP-$P2_1/c$ phase of clinoferrosilite at 35.9 GPa; (b) the configuration of O-rotated tetrahedral chain
685 with O3-O3-O3 angle of 128.7˚; (3) arrangement of $Si2O_6$ octahedra. $Fe1O_6$, $Si2O_6$ and tetrahedra SiO_4 are given in blue, yellow and
686 green, respectively. Fe2 atoms are presented as orange spheres.